Application of a Tuned Inductor in a DC Power Supply with an Active Compensation Function

Łukasz Ciepliński *[ID], Michał Gwóźdź [ID] and Rafał M. Wojciechowski [ID]

Faculty of Control, Robotics and Electrical Engineering, Poznań University of Technology, Piotrowo 3A Street, 60-965 Poznań, Poland
* Correspondence: lukasz.cieplinski@put.poznan.pl

Abstract: This work focuses on the use of a one-phase direct current (DC) power supply equipped with a shunt active filter feature, which enabled the possibility of compensation (minimisation) of reactive and distortion power, generated by a group of loads, that was connected to the same power grid node as the power supply. A tuned inductor, which was included at the input of the controlled current source (constituting the main part of the power supply) allowed for an improvement in the quality of the compensation process, compared to a device with a fixed inductive filter This resulted in a visible reduction of the nonlinear distortions of the grid current. The improvement was made possible by extending the frequency response of the current source, which allowed to increase the dynamics of the current changes at the input of the power supply. This solution represents a new approach to such power devices. This work describes the principle of operation of the proposed converter solution and presents selected test results for a laboratory model of an electric system with this device.

Keywords: converter control; tuned inductive filter; reactive power; distortion power; parallel active filter

1. Introduction

The negative impact of nonlinear loads on the operation of the power grid is a well-documented phenomenon, e.g., [1–4]. For example, commonly used conventional solutions involving power electronics devices with rectifiers (based on diodes and thyristors) and functionally simplified switched-mode power supplies cause a strongly distorted current, which results in a negative impact on the operating conditions of the power grid [5]. The most important of these impacts are an increase in power losses, a reduction in the power grid capacity, and the generation of electromagnetic disturbances. One direct effect is a reduction in the lifetimes of both the grid itself and the loads connected to it. Moreover, in addition to the technical context, this problem must be considered in terms of its economic and social (e.g., health) impacts. Hence, various types of compensators (mainly power filters, including passive, active [4,6,7], and hybrid [4,8] devices) are used in electrical systems as preventive measures. It is also worth mentioning that devices can be equipped with a power factor correction (PFC) function [4], including the widely applied DC-DC converters [9–11], which have a limited negative impact on the grid. These converters now tend to use power switches based on wide band gap materials [12]. Nowadays, wireless power transfer systems are increasingly applied (especially in the electric vehicle market) that are often characterised by PFC features [13].

So, as a result of the widely understood compensation process, the current flowing from the power grid node should have both a suitable shape and a suitable phase relation with the voltage in the power grid, depending on the compensation strategy, relative to either the reactive [14–17] or the reactive and distortion power [1,4,18]. The main disadvantage of most of these devices arises from the fact that they have only one specialised

function in the electrical system. This means that devices that are intended to improve energy quality do not perform certain tasks comprehensively; for example, they may focus on compensation, without being able to supply external loads. Existing multi-purpose devices [4,19,20] are relatively rare in electrical systems and the numerous different types of power supplies that are equipped with the additional function of a compensator are often limited to compensation of the reactive power [4,21,22].

In this work, a solution consisting of a DC power supply with an active compensation ability for both reactive and distortion power is presented. This feature is rarely found in devices of this type, especially in the case of lower power units which enable 'spread' compensation. Furthermore, the basic component of the converter, the power electronics voltage controlled current source (VCCS), is characterised by extending the frequency response. This was carried out based on a tuned inductive filter (TI), which representing a new approach to such power electronics devices. As a result, the quality of the compensation process is better, e.g., the nonlinear distortions of the grid current are lower, than in the typical solution of a parallel active filter [4], as indicated by the results of simulation [23] and laboratory tests of the power supply (PSP).

The remainder of the paper comprises six sections, which cover the issues: the basics of operation of an electrical system with a proposed power supply, an analysis of the impact of the VCCS on the operation of a power supply, the basics of operation and implementation of the TI, the structure of the device control section, the results of laboratory model tests of the electric system with the PSP, and conclusions.

2. Basics of Operation of an Electrical System with a Power Supply

When a higher current harmonic flows through the parasitic R-L elements of a power line, it causes voltage drops. Consequently, the voltage in a grid node is distorted from a sine-wave shape. The most commonly used method to compensate for this undesirable phenomenon is active filtering of the distorted current, using various types of power electronics devices. One possible type of compensator is a power supply, equipped with an active parallel filtering function. A block diagram of an electrical system (ES) containing such a device is shown in Figure 1.
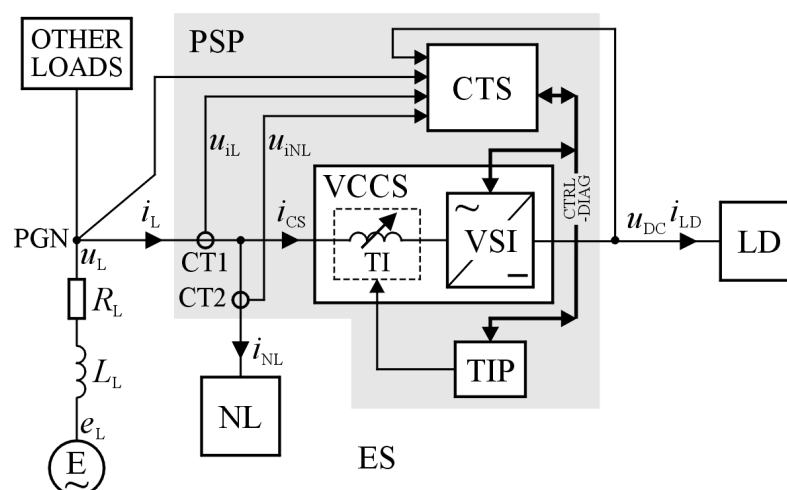

Figure 1. Block diagram of an electrical system containing a PSP equipped with a compensation function.

This system consists of the following main blocks:

- E—Power source;
- PGN—Power grid node;
- Internal resistance and inductance of the grid, R_L and L_L, respectively;
- PSP—The power supply, which forms the subject of this research. The PSP is composed of the sub-blocks: a power electronics voltage-controlled current source (VCCS), a

power stage (TIP) for the TI, and two current transducers (CT1, CT2). The PSP control section (CTS) is interconnected, via a CTRL-DIAG bus, with both the voltage source inverter (VSI), which is the internal block of the VCCS, and the TIP;

- NL—A nonlinear load;
- LD—The DC load on the PSP;
- OTHER LOADS, connected to the same power grid node.

However, in this study, it was assumed that the system was based on a one-phase power grid and the block denoted as 'OTHER LOADS' was not included.

The power theory introduced by Fryze [24] was chosen for the control of the compensation function of the PSP, although the main idea underlying the operation of the device is independent of any specific power theory. In Fryze's theory, the general aim of optimising the power grid current (i_L) is to minimise its RMS value. This results in minimisation of the power losses and an energy transfer from a source (E) to a load. The desired resultant current, flowing from the power line to the ES, can then be described by the formula:

$$i_L(t) = i_{NL}(t) + i_{CS}(t) = i_{ref,L}(t) = I_{ref,L} \sin(\omega_L t), \tag{1}$$

where i_{NL} is the current in the nonlinear load, i_{CS} is the VCCS input current, ω_L is the frequency of the voltage in the grid, and $I_{ref,L}$ is the amplitude of the reference current.

The VCCS generates a distorted current (in the general case) at its input and, when combined with the current in the nonlinear load, this theoretically results in a sinusoidal current flowing from the power line, see Equation (1). This current is in phase with the grid node voltage (u_L) [1]. As a result, the negative impact of a nonlinear load on the grid is eliminated and, in a real electric system, it is minimised. Thus, the operation of the PSP is consistent with the PFC function, with an added parallel active filtering feature.

3. Impact of the VCCS on the Operation of the PSP

The input circuit of the VCCS consists of the VSI, based on an H-type IGBT bridge [4], and an inductive filter (TI) that is included at its input, as shown in Figure 2. The IF (input filter) is a small passive band pass filter (R-L-C type) that allows for further minimisation of ripples in the VCCS input current, associated with the PWM carrier component. The IF is an optional block.
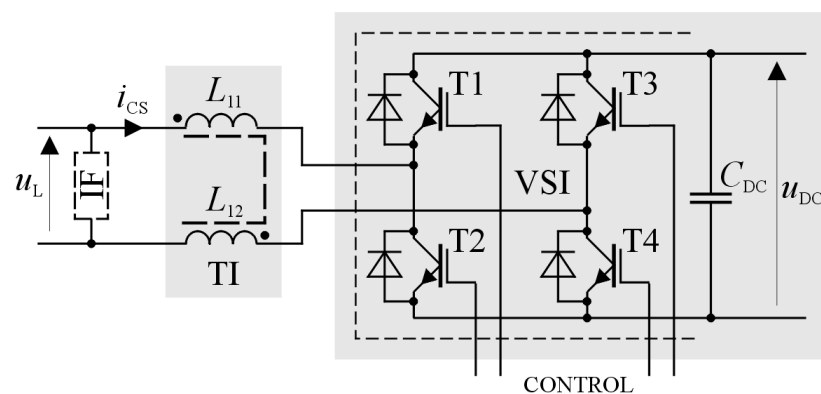

Figure 2. Diagram of the power stage of the PSP, associated with the VCCS.

Taking into account the assumed functions of the PSP, the task of the current source is not only to provide the required voltage (u_{DC}) in the DC circuit of the power supply, but also to actively compensate for the higher harmonics of the current, which are generated by the nonlinear load (NL). The role of the TI is two-fold: it increases the input impedance of the VCCS and minimises the magnitude of the input current component associated with a pulse modulation.

The TI block is composed of magnetically coupled coils. Two of these (L_{11}, L_{12}) are the main coils and the third (not shown in this figure) is the control coil. The principles of operation of the TI and the details of its design are described in Section 4.

With respect to the diagram in Figure 2, the given half-periods of the grid voltage are assumed, and appropriate pairs of transistor switches (T1-T4 or T3-T2) are turned on. The source current waveform (i_{CS}) is then described by the following general formula (omitting parasitic resistances and voltage drops at power switches in the VSI):

$$i_{CS}(t) = \frac{1}{L_{TI}} \int [u_{DC}(t) - |u_L(t)|] \mathrm{d}t, \tag{2}$$

where L_{TI} is the equivalent inductance of the TI block.

The ability of the VCCS to appropriately shape the input current is mainly determined by the frequency response, taking into account the linear model of this device. This model was analysed in previous works [23,25].

The frequency response is associated with the value of the slew-rate parameter (SR) [26,27] of the VCCS input current. According to (2), the value of SR is a direct result of the first derivative of the VCCS current, as a function of time.

Assuming that the voltage in the grid is a sine-wave, SR can be defined as:

$$SR = \frac{1}{L_{TI}} [u_{DC}(t) - |U_L \sin(\omega_L t)|], \tag{3}$$

where U_L is the amplitude of the grid voltage.

Hence, in this case, SR depends on the instantaneous value of the grid voltage, among other things. SR reaches two extreme values, which are given by the equations:

$$SR_{max} = \frac{1}{L_{TI}} u_{DC}(t_0)|_{t_i = i\frac{\pi}{\omega_L}} : i = 0, \pm 1, \pm 2,\ldots, \tag{4}$$

and

$$SR_{min} = \frac{1}{L_{TI}} [u_{DC}(t_0) - U_L]|_{t_i = (\frac{1}{2}+i)\frac{\pi}{\omega_L}} : i = 0, \pm 1, \pm 2,\ldots \tag{5}$$

Equations (4) and (5) indicate that the VCCS has the highest dynamics when the instantaneous value of the grid voltage passes through zero and the lowest dynamics when this voltage reaches the maximum value. Since both the value of the grid voltage and the voltage in the DC circuit of the power supply are set in advance, the only factor that can enlarge the frequency response of the VCCS is the filter inductance. However, lowering this value will result in an increase in the amplitude of the pulse modulation carrier component of the PSP input current. Hence, in order to increase the frequency response of the current source, the use of an inductive filter with a variable inductance value was proposed. This solution allows for a better approximation of the shape of the grid current to the ideal waveform, imposed by (1), in a situation of highly dynamic changes in the i_{NL} current, compared to a VCCS with a filter with a fixed inductance value. At the same time, in the steady state of operation of the PSP, the magnitude of the pulse modulation carrier component in the PSP input current remains at the minimum assumed level.

4. Tuned Inductive Filter

4.1. Principle of Operation of the Filter

To implement the tuned inductive filter, the phenomenon of coupling between the magnetic fluxes of coils was exploited. As a consequence of the operation of this circuit, the resultant magnetic flux can be amplified or reduced, which also results in a change in its equivalent inductance (reactance). Thus, the value of the equivalent reactance (X_{TI}) of the inductor can reach two values, depending on the state of the S switch, see Figure 3. The parameter L_1 in the figure is associated with the main (primary) winding of the inductor, while L_2 is related to the control (secondary) winding.
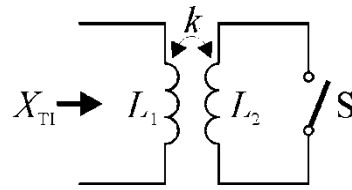
Figure 3. Diagram of the operating principle of a tunable inductive filter.

The value of the equivalent inductance of the filter was determined based on the assumption that the (homogeneous) ferromagnetic core, on which the coils are wound, is linear. Moreover, the resistances of both coils are omitted. The following equation was obtained in previous work [25], in which the value of X_{TI} is dependent on both the magnetic coupling factor of the coils (k) and the state of the S-switch:

$$X_{TI} = \left(1 - S_{T\text{-}TI}k^2\right)X_1\Big|_{0 \le k \le 1,\ S_{T\text{-}TI}=0\ \lor\ S_{T\text{-}TI}=1}, \tag{6}$$

where X_1 is the reactance of the primary winding, $S_{T\text{-}TI} = 0$ when the switch is open, and $S_{T\text{-}TI} = 1$ when the switch is closed.

4.2. Simulation Studies of the Filter Model

Detailed simulation studies of the implementation of the tuned filter were conducted in a Maxwell environment. To achieve the assumed value of the equivalent inductance in both states of the switch, a sophisticated design of the magnetic circuit of the inductor was necessary. As a result of these studies, a model of the inductor was based on a three-winding transformer with a working air gap, see Figure 4a.
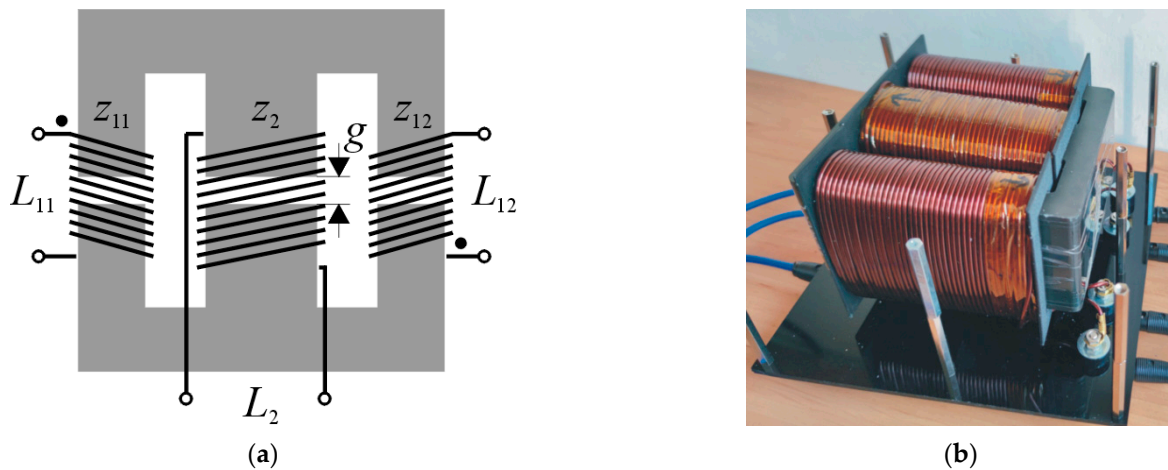

(**a**)

(**b**)

Figure 4. Details of the tuned inductor design (**a**) and its general view (**b**).

A 3D field model of the TI was used to determine the optimal values of the number of turns (z_{11}, z_{12}, and z_2, with the assumption that: $z_{11} = z_{12} = z_2$). The width of the air gap (g), for which the reactance ratio of the inductor is defined as:

$$x_{TI} = \frac{X_{TI}\big|_{S_{T\text{-}TI}=0}}{X_{TI}\big|_{S_{T\text{-}TI}=1}}, \tag{7}$$

should be close to 3.0 and so, based on Equation (6), k should be close to 0.82.

The assumption was made that the value of the equivalent inductance ($L_{TI} = L_{11} + L_{12}$—Figures 2 and 4a) for both states of S should be in the range of 1–5 mH. The listed values were chosen as a result of extensive simulation studies of the PSP, conducted in the SPICE/ORCAD environment, as a compromise between a possible increase in the VCCS

dynamics and minimisation of the pulse modulation component, which causes ripples in the input current. In order to obtain the desired value of x_{TI}, in relation to the desired parameter values, the interval search method [28] was used, and this was implemented using the optimisation module in Maxwell software. The method consisted of searching for the best value of the objective function (in this case, the appropriate value of x_{TI}) by systematically searching the range of values for the parameter g and the number of turns. The general view of the laboratory model of the inductor is shown in Figure 4b.

4.3. Laboratory Tests of the Filter

The implementation of the filter in the PSP is shown in Figure 5. The TIP block corresponds to the same block in Figure 1.
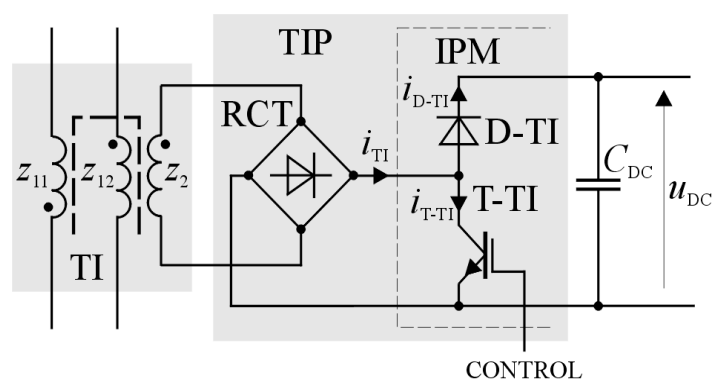

Figure 5. Diagram showing the implementation of the tuned inductor in the model of the PSP (RCT—fast diode rectifier).

The basic technical parameters of the tuned inductor are as follows:

- Magnetic core: Four E-shapes (OT49928EC) of T-type material, manufactured by MAGNETICS Inc. [29];
- Number of turns: $z_{11} = z_{12} = z_2 = 80$;
- Width of the air gap g = 1.5 mm;
- Inductance over a quasi-linear range of operation of the magnetic core: 4.70 mH with secondary winding open, and 1.45 mH with secondary winding short-circuited;
- Maximum magnitude of the filter current over the quasi-linear range of operation of the core: 20 A;
- Resistance of the single winding: 110 mΩ.

In the one-phase version of the PSP, the role of the branch with the T-TI and D-TI devices can be played by the third branch of the IGBT module. These modules are typically manufactured as three-branch devices (or three branches plus a 'braking' branch) [30]. This gives the proposed solution a clear economic value.

5. Structure of the PSP Control Section

The block diagram of the power supply control section (CTS) is shown in Figure 6.
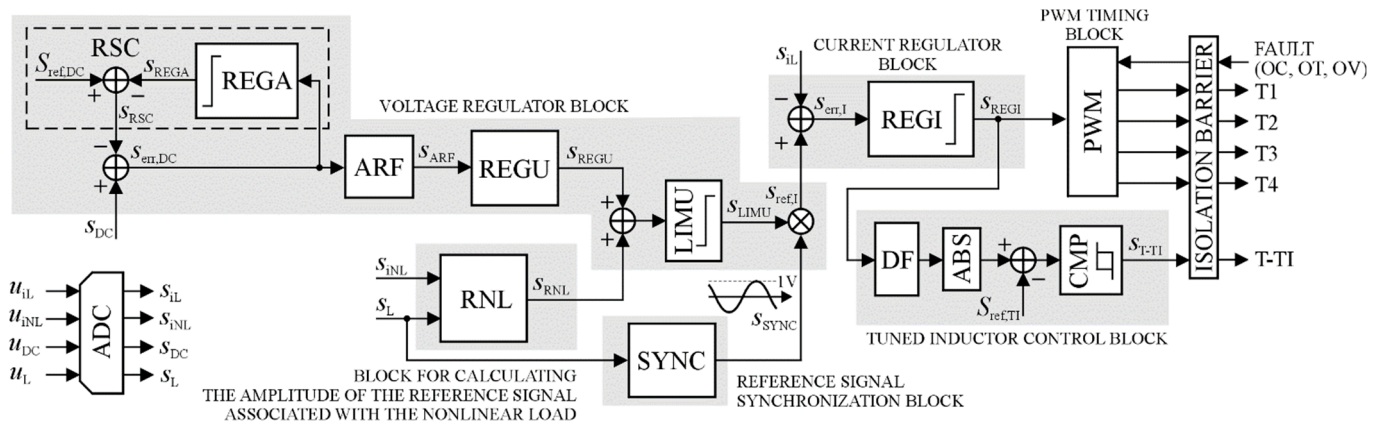
Figure 6. Block diagram of the power supply control section.

The control algorithm consists of five main blocks, each of which contains between one and four internal sub-blocks, which are shown on a grey background. The CTS was implemented using the ALS-G3-1369 Evaluation Board [31], equipped with an ADSP-21369 floating-point digital signal processor (DSP) from Analog Devices Inc. [32]. This board is specialised for such power electronics applications that require a CPU with high computational power and a high resolution of the PWM pattern, among other things. This platform also contains multi-channel AD and DA converters (ADC and DAC, respectively). In this case, the ADC forms the input ports for the external signals u_L, u_{iL}, u_{iNL}, and u_{DC}. All internal digital signals in the CTS are denoted with the prefix . The PWM timing block is denoted as PWM. Due to the limitations on the computing power of each processor, and in view of the high complexity of the control algorithm, the external signals were sampled at two different frequencies: u_L, u_{iNL}, and u_{DC} was sampled at $f_{S,1}$, while u_{iL} was sampled at $f_{S,2}$, where $f_{S,2} >> f_{S,1}$. This was necessary due to the requirement for high precision in the control of the transient process in the PSP input current, i_L ($u_{iL} = r_{CT1}i_L$, r_{CT1}—transfer ratio of the CT1).

The entire control algorithm was written in the C-language. The C/C++ compiler is an integral part of VisualDSP++, the development environment for Analog Devices processors.

5.1. Calculation of the Reference Signal for the Nonlinear Load (RNL Block)

Both the structure and operating rules of the RNL block are related to the compensation function of the PSP. The role of the block is to generate the s_{RNL} signal, which is associated with the current value of the active power of the NL. The value of this signal is calculated based on the external signals u_L and $u_{iNL} = r_{CT2}i_{NL}$, where r_{CT2} is the transfer ratio of the CT2. The s_{RNL} is then added to the output signal of the voltage regulator, s_{REGU}. Hence, s_{REGU} directly affects the amplitude of the reference signal $s_{ref,I}$ for the current regulator block. The waveform s_{RNL} is a step function of the time, i.e., it has a constant value over a half-period of the grid voltage-synchronous signal (s_{SYNC}), which prevents strong distortion of $s_{ref,I}$ from the sine-wave.

5.2. Reference Signal Synchronisation Block (SYNC)

The role of this block is to generate the sine-wave signal (s_{SYNC}) with a unity value amplitude, which is in phase with the first harmonics of the voltage waveform in the grid node: $s_{SYNC}(t) = \sin(\omega_L t)$. The details of operation of the SYNC block were presented in previous work [33].

5.3. Voltage Regulator Block

This block is responsible for control of the voltage in the DC circuit of the PSP, and contains the following sub-blocks:

- ARF (anti-ripple filter). This is an FIR-type filter, the role of which depends on both the elimination of the error signal ($s_{err,DC}$) at the input of the REGU, the ripples associated with the u_{DC} voltage and computing the true average value of the DC voltage. The ripples are caused by the grid voltage waveform and may appear in the error signal ($s_{err,DC}$), since this also operates at the DC voltage. Without the ARF block, the ripples in the error signal would strongly distort the reference signal for the current regulator ($s_{ref,I}$) from a desired sine-wave shape. The magnitude part of the ARF transfer function is given by Equation (8) [16]:

$$|H_{ARF}(f)| = \left| \cos\left(\frac{\pi}{2} \frac{f}{f_{ARF}} \right) \right|, \tag{8}$$

where $f_{ARF} = \frac{\omega_L}{\pi}$ is the characteristic frequency of the filter.

- RSC (reference signal correction block). The idea underlying the operation of the RSC is based on the work presented in [34]. However, there are some essential differences. The RSC processes both the reference signal for the master voltage regulator (REGU), i.e., $S_{ref,DC}$, and the error signal ($s_{err,DC}$) associated with this regulator. The RSC output signal (s_{SRC}) is a value-corrected right reference signal ($S_{ref,DC}$) for the REGU. A basic description of the operation of the RSC is given in the time domain which, in this case, is more convenient than a description in the frequency domain. Assuming $S_{ref,DC}$ = constant, gives:

$$s_{RSC}(t) = S_{ref,DC} - s_{err,DC}(t) * h_{REGA}(t) = \\ = S_{ref,DC} - [s_{DC}(t) - s_{RSC}(t)] * h_{REGA}(t) \tag{9}$$

where $h_{REGA}(t)$ is the pulse response of the RSC internal regulator (REGA) and * represents the convolution.

Respecting the impact of the operation of the RSC block on the stability of the PSP (based on the linear model of this device [23]), the REGA block was implemented as a first-order low-pass filter. In this case, Equation (9) takes the form:

$$s_{DC}(t) = S_{ref,DC} \left[1 - e^{\left(-\frac{t}{\tau_{REGA}} \right)} \right] \overset{t \to \infty}{\to} S_{ref,DC}. \tag{10}$$

In other words, the value of the control error, associated with the average value of the DC voltage, in the steady state of the system, theoretically tends to zero.

- REGU (regulator of the voltage in the DC circuit). On the basis of the simulation model tests [23], a P-type REGU was chosen. The REGU output signal (s_{REGU}) is added to the signal generated in the RNL block, s_{RNL}. The sum of these two signals sets the value of the amplitude of the reference signal for the current regulator ($s_{ref,I}$).
- LIMU (limiter of the voltage regulator output signal magnitude). This imposes the maximum value of the current at the input of the VCCS, respecting both the rated current of the IGBT power module and the maximum current in the quasi-linear range of operation of the tuned inductor.

5.4. Current Regulator Block

This block is responsible for controlling the VCCS input current. The main task of the regulator is to provide a LAG-type correction [26,27] of the 'transfer function' of the VCCS. A combination of P and PI topology, referred to here as P2I, was chosen for the REGI block:

$$T_{REGI}(s) = k_{I,0} \frac{j\frac{s}{\omega_{I,2}} + 1}{j\frac{s}{\omega_{I,1}} + 1}, \tag{11}$$

where $k_{I,0}$ is the regulator gain for DC, $\omega_{I,1}$ and $\omega_{I,2}$ are the characteristic frequencies, and $\omega_{I,2} > \omega_{I,1}$.

Compared to the PI regulator, the proposed regulator introduces a much smaller phase shift over a wider frequency range. The gain value of P2I at the power line frequency of 50 Hz is comparable with that of a PI regulator. Above the characteristic frequency of $f_{I,1}$, the gain plots for P2I and PI are very similar while, above the characteristic frequency of $f_{I,2}$, the phase plots are also comparable. The values of the regulator settings and the settings of the other blocks in the CTS were determined based on a small-signal model of the device [23,25] and the original program in the C-language, in which this model was applied. In this case, the Nyquist criterion was used to evaluate the asymptotic stability of the system [26,27].

In addition to regulating the input current of the VCCS, another task of the REGI is to minimise the PWM components (at a frequency of about $2f_c$) in its output signal, the presence of which can lead to deterministic chaos [35] that can disturb the entire regulation process.

The REGI is also equipped with a signal magnitude limiter at the output, which prevents the PWM block from entering into an over-modulated state.

5.5. Tuned Inductor Control Block

The TI control block (TIC) is responsible for generating the pulse-duration modulated signal ($s_{T\text{-}TI}$), which controls the T-TI switch. This block consists of two main sub-blocks:

- ABS—This calculates the absolute value of the input signal.
- DF—Decimation Filter. The dynamic limitations of the real S-switch were respected by selecting the value of the decimation factor (DF).
- CMP—This is the hysteresis comparator, which operates on a signal composed of the difference between the ABS output signal and the reference signal for the TIC block ($S_{\text{ref,TI}}$); it generates the S-switch control signal.

6. Laboratory Tests of the Electrical System

6.1. Arrangement of the Laboratory Setup

The general view of the laboratory arrangement of the ES during the tests is shown in Figure 7. In the power stage of the PSP, a P3-5-550MFE LABINVERTER was used [31]. This laboratory-scale, multi-purpose power electronics converter was developed for advanced R&D applications.
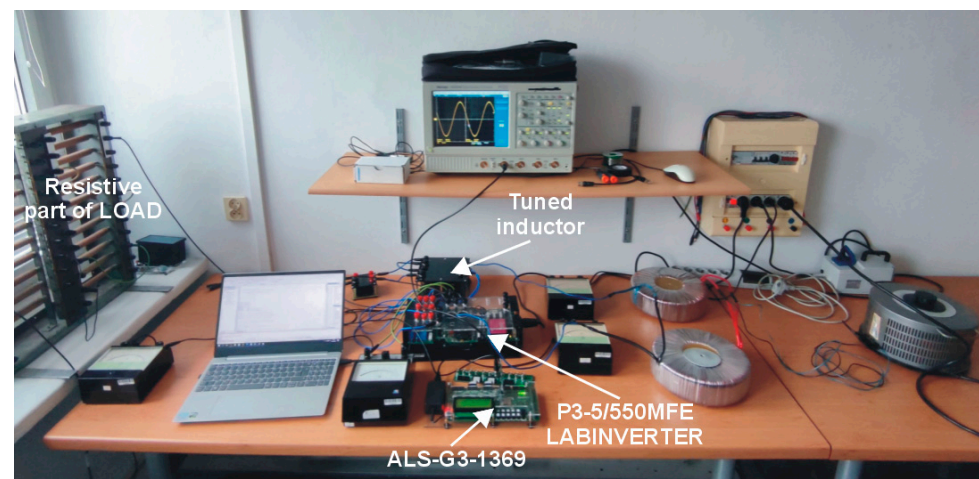

Figure 7. General view of the laboratory setup.

The main parameters of the laboratory model of the ES, and their values during the tests, are listed in Table 1.

Table 1. List of Basic Parameters of the ES Laboratory Model.

No.	Parameter Name	Parameter Symbol	Parameter Value
	General PSP parameters		
1	Nominal power grid voltage	-	230 V
2	Grid resistance	R_L	0.5 Ω
3	Grid inductance	L_L	320 μH
4	Nominal DC output power	-	1.5 kW
5	Rated DC voltage and range of settings of the voltage	-	400 ($\pm$25) V
6	Maximum magnitude of the VCCS input current	-	20 A
7	Sampling frequency (1) in CTS	$f_{S,1}$	20 kHz
8	Sampling frequency (2) in CTS	$f_{S,2}$	100 kHz
	Power stage of the VCCS		
9	Capacitance of the capacitor in the DC circuit	C_{DC}	1 mF
10	PWM carrier frequency	-	10 kHz
	CTS—voltage regulator		
11	Characteristic frequency of the ARF	f_{ARF}	100 Hz
12	Gain of the REGU	$k_{U,0}$	0.25
13	Gain of the REGA	$k_{A,0}$	0.99
14	Time constant of the REGA	τ_{REGA}	10 ms
15	Signal clipping level in LIMA	$A_{L,A}$	$\pm$50 V
16	Reference signal for RSC block	$S_{ref,DC}$	400 ($\pm$25) V
17	Signal clipping level in LIMU	$A_{L,U}$	$\pm$15 V
	CTS—Current regulator		
18	Gain	$k_{I,0}$	1000 V/V
19	Characteristic frequency	$f_{I,1}$	97 Hz
20	Characteristic frequency	$f_{I,2}$	1.16 kHz
21	Signal clipping level	$A_{L,I}$	$\pm$450 V
	CTS—Tuned inductor control block		
22	Reference signal for the CMP block	$S_{ref,TI}$	380 V
23	Decimation factor of the DF	DF	1

6.2. Laboratory Tests and Discussion

A set of tests of the PSP control algorithm and the ES as a whole were conducted using hardware-in-the-loop (HIL) modelling. Most of the waveforms were obtained using the PLOT function of VisualDSP++ [32], which allows for the graphic visualisation of numerical data (e.g., waveforms) stored in arrays (via a dedicated graphical interface, operating in WINDOWS OS) and a scope.

During these investigations, a number of tests were performed for various types of NL load. However, only some of these results are presented. They are related to the type of non-linear load which is the most demanding for the efficiency of the PSP's work as a compensator. These tests involved the NL block as the thyristor voltage regulator with the firing angle set to 90 electric degrees, loaded by the resistor, with only parasitic serial inductance included. In this case of the NL block, the characteristic waveforms of voltage and current are shown in Figure 8. Also, the waveform of the grid voltage-synchronous signal (s_{SYNC}) is shown.
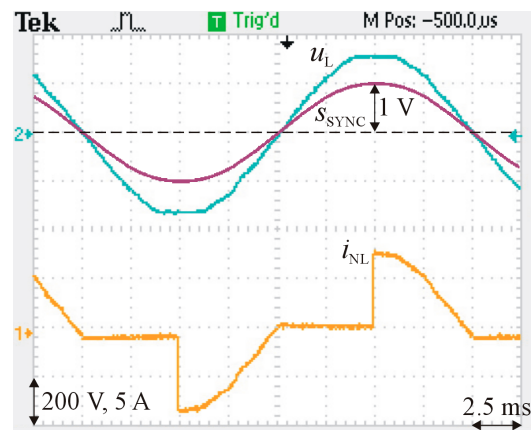
Figure 8. Waveforms of the grid voltage and NL current for a real, 'soft' power grid and the grid voltage–synchronous signal, at the output of the SYNC block.

In the following section, selected waveforms are presented which are characteristic of the operation of the ES laboratory model. In this case, the DC voltage was set to 375 V, the lowest achievable value in the model of PSP. The nonlinear distortion factor of the NL block current was approximately 65%. The PSP output power at the DC side was equal to the rated value, while the power of the NL block was set at approximately 50% of the rated PSP power. In the case of the PSP input current, shown in Figure 9, the compensation function was disabled. In turn, Figure 10 shows the tests results when the compensation function of the power supply was turned on. In Figure 10b (lower plot), the waveform of the current regulator output signal and the S-switch control signal, for the transient state of the PSP input current, are presented (in the magnified portion of the drawing).
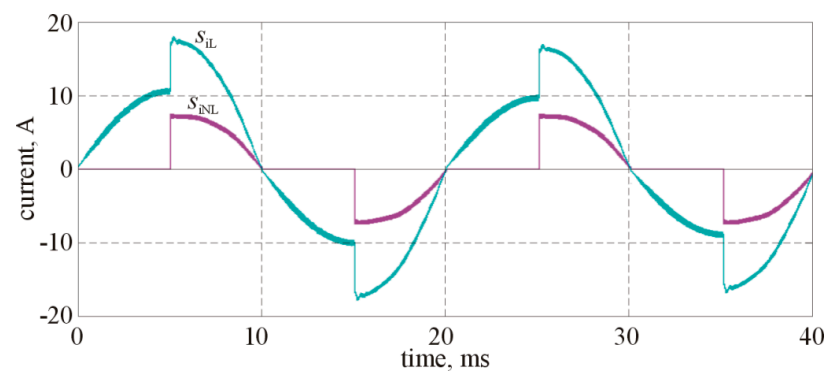

Figure 9. Waveforms for the PSP input current and nonlinear load current when the PSP compensation function was disabled.
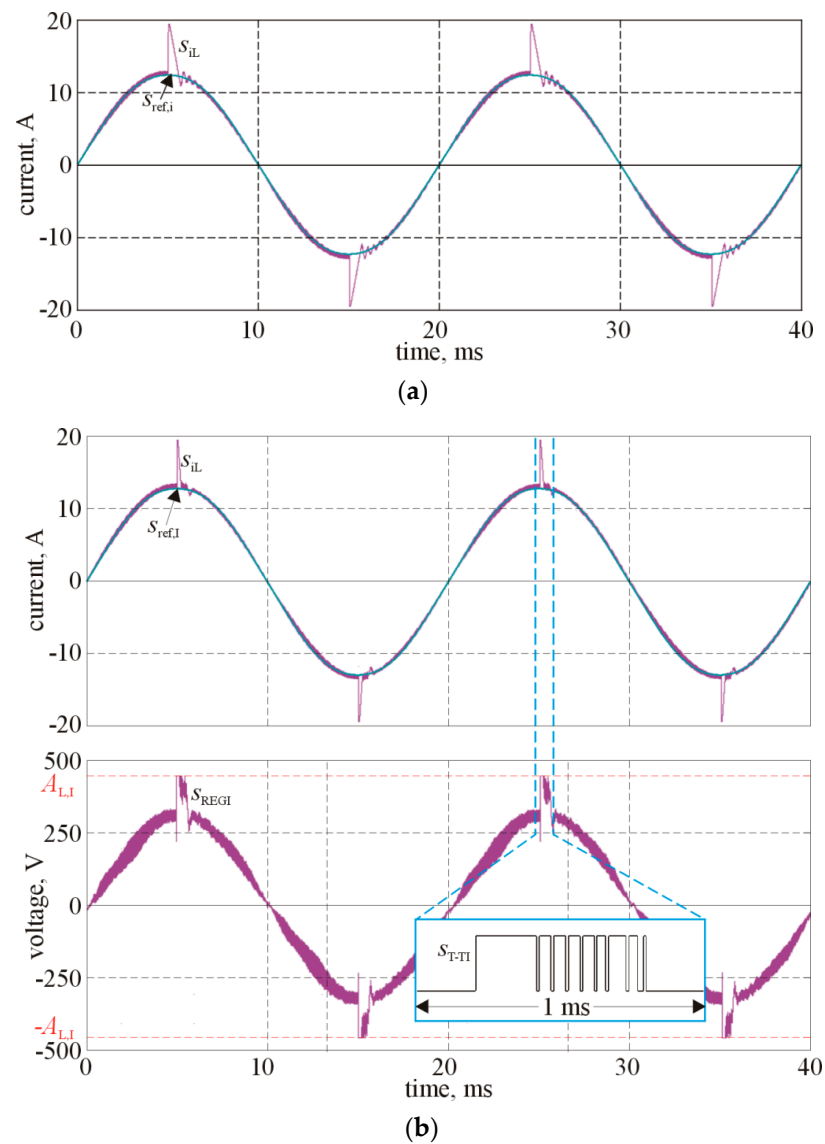
Figure 10. Waveforms in the PSP when the compensation function is enabled with (**a**) a fixed and (**b**) a tuned inductor.

As the basic quantities characterising the quality of operation of the PSP compensation function, the values of $TTHD$ for the PSP input current (i_L) and the duration of the transient state in this current (τ_T) were recorded. The values of both parameters are shown as curves in Figure 11, relative to the value of the set DC voltage. Additionally, this figure presents the value of THD coefficient, calculated with respecting up to the 50th harmonics. These results show an improvement by a factor of 1.4–1.6, in relation to the $TTHD$, and by a factor of 2.3–2.5, in relation to the τ_T, in the PSP input current quality, as a result of the PSP operation with the TI.
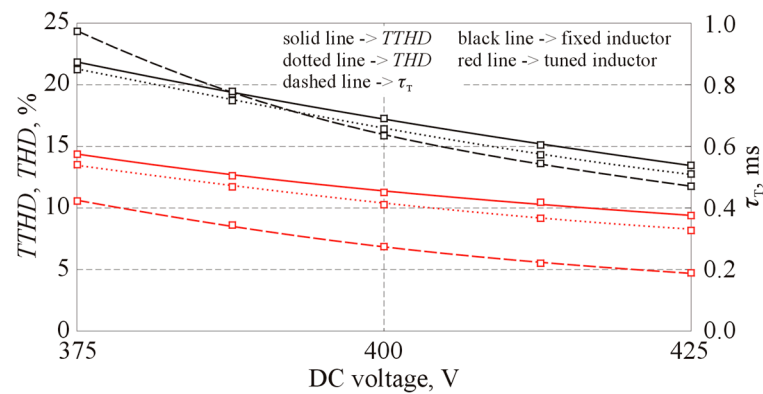
Figure 11. Curves for $TTHD$, THD, and τ_T vs. The DC voltage.

Figure 12 shows a set of characteristic waveforms, associated with the response of the PSP to step changes in the DC load. The transient state of the DC voltage was equal to 2.5 periods of the line voltage. In the steady state of the system, the average value of the DC voltage was close to the value of the reference signal; within the full range of DC voltage settings (Table 1), the average value of the DC voltage control error, associated with the DC voltage regulator block, was lower than 1 V.
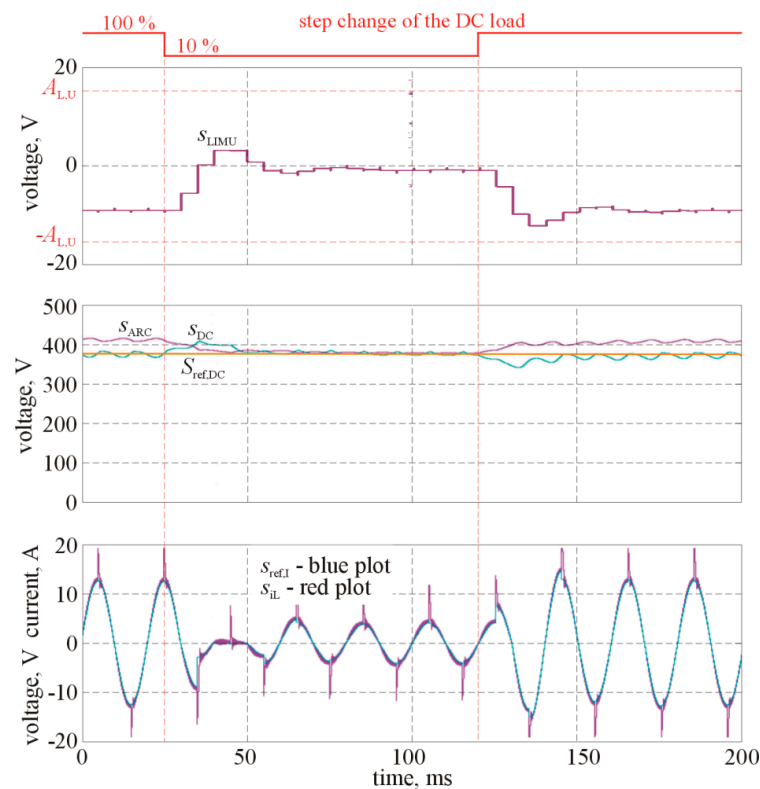

Figure 12. Waveforms in the PSP in response to step changes in the DC load. The upper plot shows the signal at the output of the voltage regulator, the middle plot shows signals related to the DC circuit, and the lower plot shows the reference signal for the current regulator and PSP input current.

7. Conclusions

The main aim of this research was to verify the operation of the proposed PSP in an external electrical system. A set of laboratory tests of a system containing this device were performed and the results confirmed the high effectiveness of operating the proposed solution as a part of this system. The use of a tuned inductor allowed the power supply to

increase the dynamics of the PSP input current changes in relation to a system with a fixed value of inductance. According to the criteria use, the results of these experiments show an improvement in the quality of the PSP input current, by a factor of 1.5–2.4, on average, when the TI filter was applied. The algorithm implemented in the PSP control section (mainly in relation to the RSC block) also made it possible to obtain high-quality regulation processing of the DC voltage; the value of the DC error was equal to approximately 0.2% of the reference voltage (independent of the values of both the DC voltage and the PSP output power). The duration of the transient state after a step change in the DC load did not exceed 2.5 periods of the line voltage (in this case, 50 ms). Moreover, the use of a tuned inductor had no visible impact on the quality of voltage regulation in the DC circuit.

For a small degree of increase in both the hardware and software complexity of the proposed solution of the power supply, compared to a system without a compensation function, this device appears to be an economical alternative for functionally specialised active filters.

Author Contributions: Conceptualization, M.G.; methodology, M.G. and R.M.W.; software, M.G. and Ł.C.; validation, Ł.C. and R.M.W.; formal analysis, M.G. and R.M.W.; investigation, M.G., Ł.C. and R.M.W.; resources, Ł.C.; data curation, M.G.; writing—original draft preparation, M.G.; writing—review and editing, M.G., Ł.C. and R.M.W.; visualization, M.G. and Ł.C. All authors have read and agreed to the published version of the manuscript.

Institutional Review Board Statement: Not applicable.

Informed Consent Statement: Not applicable.

Conflicts of Interest: The authors declare no conflict of interest.

References

1. Akagi, H.; Watanabe, E.H.; Aredes, M. *Instantaneous Power Theory and Applications to Power Conditioning*; John Wiley & Sons: Hoboken, NJ, USA, 2017; ISBN 9781118362105.
2. Parhizi, S.; Lotfi, H.; Khodaei, A.; Bahramirad, S. State of the art in research on microgrids: A review. *IEEE Access* **2015**, *3*, 890–925. [CrossRef]
3. Ma, Y.; Hong, F.; Zhou, X.; Gao, Z. An overview on harmonic suppression. In Proceedings of the 2018 Chinese Control and Decision Conference (CCDC), Shenyang, China; 2018; pp. 4943–4948. [CrossRef]
4. Rashid, M.H. *Power Electronics Handbook*; Elsevier Ltd.: Oxford, UK, 2018; ISBN 0-12-581650-2.
5. Masetti, C. Revision of European standard EN 50160 on power quality: Reasons and solutions. In Proceedings of the 14th International Conference on Harmonics and Quality of Power-ICHQP, Bergamo, Italy, 26–29 September 2010.
6. Vahedi, H.; Shojaei, A.A.; Dessaint, L.; Al-Haddad, K. Reduced DC-link voltage active power filter using modified PUC5 converter. *IEEE Trans. Power Electron.* **2018**, *33*, 943–947. [CrossRef]
7. Trinh, Q.; Lee, H. An enhanced grid current compensator for grid-connected distributed generation under nonlinear loads and grid voltage distortions. *IEEE Trans. Ind. Electron.* **2014**, *61*, 6528–6537. [CrossRef]
8. Ye, T.; Dai, N.; Zhu, M. Optimize the series LC design of a quasi proportional-resonant controlled hybrid active power filter for harmonic compensation. In Proceedings of the 2016 IEEE 11th Conference on Industrial Electronics and Applications (ICIEA), Hefei, China, 5–7 June 2016; pp. 624–629. [CrossRef]
9. Onal, Y.; Sozer, Y. Bridgeless SEPIC PFC converter for low total harmonic distortion and high power factor. In Proceedings of the 2016 IEEE Applied Power Electronics Conference and Exposition (APEC), Long Beach, CA, USA, 20–24 March 2016; pp. 2693–2699.
10. Lee, S.; Do, H. A single-switch AC–DC LED driver based on a boost-flyback PFC converter with lossless snubber. *IEEE Trans. Power Electron.* **2017**, *32*, 1375–1384. [CrossRef]
11. Yang, C.; Liu, Y.; Tseng, P.; Pan, T.; Chiu, H.; Lo, Y. DSP-based interleaved buck power factor corrector with adaptive slope compensation. *IEEE Trans. Ind. Electron.* **2015**, *62*, 4665–4677. [CrossRef]
12. Huang, Q.; Huang, A.Q. Review of GaN totem-pole bridgeless PFC. *CPSS Trans. Power Electron. Appl.* **2017**, *2*, 187–196. [CrossRef]
13. Liu, J.; Xu, W.; Chan, K.W.; Liu, M.; Zhang, X.; Chan, N.H.L. A three-phase single-stage AC–DC wireless-power-transfer converter with power factor correction and bus voltage control. *IEEE J. Emerg. Sel. Top. Power Electron.* **2020**, *8*, 1782–1800. [CrossRef]
14. Benchabira, A.; Khiat, M. A hybrid method for the optimal reactive power dispatch and the control of voltages in an electrical energy network. *Arch. Electr. Eng.* **2019**, *68*, 535–551.
15. Qiao, X.; Bian, J.; Chen, C.; Li, H. Comparison and analysis of reactive power compensation strategy in power system. In Proceedings of the 2019 IEEE Sustainable Power and Energy Conference (iSPEC), Beijing, China, 21–23 November 2019; pp. 689–692. [CrossRef]

16. Lee, Y.; Song, H. A reactive power compensation strategy for voltage stability challenges in the Korean power system with dynamic loads. *Sustainability* **2019**, *11*, 326. [CrossRef]

17. Czarnecki, L.; Almousa, M. Adaptive balancing by reactive compensators of three-phase linear loads supplied by nonsinusoidal voltage from four-wire lines. *Am. J. Electr. Power Energy Syst.* **2021**, *10*, 32–42. [CrossRef]

18. Pasko, M.; Buła, D.; Dębowski, K.; Grabowski, D.; Maciążek, M. Selected methods for improving operating conditions of three-phase systems working in the presence of current and voltage deformation—Part I. *Arch. Electr. Eng.* **2018**, *67*, 591–602.

19. Antoniewicz, K.; Rafal, K. Model predictive current control method for four-leg three-level converter operating as shunt active power filter and grid connected inverter. *Bull. Pol. Acad. Tech.* **2017**, *65*, 601–607. [CrossRef]

20. Śleszyński, W.; Cichowski, A.; Mysiak, P. Current harmonic controller in multiple reference frames for series active power filter integrated with 18-pulse diode rectifier. *Bull. Pol. Acad. Tech.* **2018**, *66*, 699–704.

21. Bednarek, K. Compensation of reactive power and hybrid operation in the systems of uninterruptible power supply (UPS). *Comput. Appl. Electr. Eng.* **2013**, *11*, 209–221.

22. Zajkowski, K. Reactive power compensation in a three phase power supply system in an electric vehicle charging station. *J. Mech. Energy Eng.* **2018**, *2*, 75–84. [CrossRef]

23. Gwóźdź, M.; Ciepliński, Ł.; Krystkowiak, M. Power supply with parallel reactive and distortion power compensation and tunable inductive filter—Part 1. *Bull. Pol. Acad. Tech.* **2020**, *68*, 401–408.

24. Depenbrock, M.; Marshal, D.A.; Wyk, J.D. Formulating requirements for universally applicable power theory as control algorithm in power compensators. *Eur. Trans. Elect. Power ETEP* **1994**, *4*, 445–456. [CrossRef]

25. Gwóźdź, M. Stability of discrete time systems on base of generalized sampling expansion. *Q. Elektr. Silesian Univ. Technol.* **2011**, *1*, 29–40.

26. Doyle, J.C.; Francis, B.A.; Tannenbaum, A.R. *Feedback Control Theory*; Dover Publications: Mineola, NY, USA, 2013; ISBN 130632548X.

27. Bentsman, J. *Introduction to Signal Processing, Instrumentation, and Control: An Integrative Approach*; World Scientific Publishing: Singapore, 2016.

28. Saeed, S.; Georgious, R.; Garcia, J. Modeling of magnetic elements including losses application to variable inductor. *Energies* **2020**, *13*, 1865. [CrossRef]

29. Soft Magnetic Components: Powder Cores & More. Available online: https://www.mag-inc.com/home (accessed on 5 February 2021).

30. Mitsubishi Electric, Intelligent Power Modules. Available online: http://www.mitsubishielectric.com/semiconductors/products/powermod/intelligentpmod/index.html (accessed on 5 February 2021).

31. Available online: http://analog.alfine.pl/oferta/produkty-alfine/systemy-uruchomieniowe (accessed on 5 February 2021).

32. Available online: https://www.analog.com/en/products/adsp-21369.html#product-documentation (accessed on 5 February 2021).

33. Gwóźdź, M.; Ciepliński, Ł. An algorithm for calculation and extraction of the grid voltage component. *Energies* **2021**, *14*, 4842. [CrossRef]

34. Pop, S.; Pitica, D.; Ciascai, I. Adaptive algorithm for error correction from sensor measurement. In Proceedings of the 2008 31st International Spring Seminar on Electronics Technology, Budapest, Hungary, 7–11 May 2008; pp. 373–378. [CrossRef]

35. Vaidyanathan, S.; Volos, C. *Advances and Applications in Chaotic Systems*; Springer: Berlin/Heidelberg, Germany, 2016. [CrossRef]